A study on the capabilities and accuracy of Kapton based TOF space dust and debris detectors

L.T. Cornwell [a,*], P.J. Wozniakiewicz [a,*], M.J. Burchell [a], L.S. Alesbrook [a],
R.D. Corsaro [b], F. Giovane [c], J.-C. Liou [d]

[a] Centre for Astrophysics and Planetary Science, School of Physical Sciences, Univ. of Kent, Canterbury CT2 7NH, United Kingdom
[b] AstroAcoustics, 201 DeLa Gaye Pt, Beaufort, SC 29902, USA
[c] Giovane Consultants, 576 Glebe View Lane, Lottsburg, VA 22511, USA
[d] NASA Orbital Debris Program Office, NASA Johnson Space Center, Houston, TX 77058, USA

Abstract

The growing population of space debris in the near-Earth environment means there is an increased need for space-based detectors, capable of measuring and distinguishing natural space dust and anthropogenic orbital debris populations, to monitor and quantify the relative threat they pose. This has led to much research into the development of new detectors, including those based on time of flight (TOF) designs which can give impact speed and direction. Kapton's favourable properties (e.g. its low mass and ability to be manufactured as thin films) and tried and tested space applications, suggest it may be suitable for use in TOF detectors where impactor speed is measured by passage through several films with known separation. To test the measurement accuracy of such a detector, a prototype Kapton based TOF space dust and debris detector was constructed, and impacted at 2 and 4 km s^{-1}. For a Kapton film thickness of 12.5 μm and projectiles of 1 mm in size, within experimental uncertainties of ~1%, there was no difference between incident projectile speed (as measured independently) and that measured by the TOF detector. This, confirms that Kapton based TOF detectors are capable of measuring particle speed to a high degree of accuracy, making them suitable for measuring the near-Earth particle environment.
© 2022 COSPAR. Published by Elsevier B.V. This is an open access article under the CC BY license (http://creativecommons.org/licenses/by/4.0/).

1. Introduction

Interplanetary dust has major scientific value to the space science community. It is largely thought to originate from comets and asteroids, thus provides information regarding the constituents, conditions, and processes taking place on these parent bodies (Grün et al., 2001; Wozniakiewicz, 2017; Grün et al., 2019). It is even possible that some of the dust can have an interstellar origin and thus offer insights into wider processes (e.g. Dorschner (2001), Draine (2003), Strub et al. (2019)). As well as the natural cosmic dust, ever since the first human activities in space, in the 1950's, an ever-increasing component of the near-Earth dust environment is the population of anthropogenic orbital debris (e.g. see Wozniakiewicz and Burchell (2019) for a recent review). This population is increasing significantly; in 2006 there were ~9000 pieces of orbital debris greater than 10 cm in size being tracked by the U.S Space Surveillance Network (SSN) (Liou, 2006), whereas in 2021 more than 22,000 pieces of orbital debris were being tracked by the SSN (NASA, 2021a). This trackable debris requires spacecraft to perform avoidance

* Corresponding authors.
    E-mail addresses: L.T.Cornwell@kent.ac.uk (L.T. Cornwell),
P.J.Wozniakiewicz@kent.ac.uk (P.J. Wozniakiewicz).

manoeuvres whenever a high-risk conjunction occurs (NASA, 2020) to mitigate the risk of a catastrophic collision (NASA, 2021b). In addition, there is far more debris <10 cm in size that cannot be tracked from the Earth, from which spacecraft require shielding. As such, orbital debris represents a significant threat to spacecraft, with even millimetre-sized debris able to cause fatal damage due to the high speed at which they impact (mean impact speeds are in the range 7 to 14 km s^{-1} in low earth orbit (Kessler et al., 1989; Burchell et al., 2013)). To shield spacecraft from this threat, address the problem of orbital debris and improve sustainability in space, an accurate measure of the debris environment is required.

A corollary of the above is the need for space-based detectors that can detect and differentiate between both interplanetary dust and orbital debris. The best means of achieving this is to measure the speed and direction of the incident particle to determine whether the trajectory matches that of an orbital debris particle, ∼7 to 14 km s^{-1}, or an interplanetary dust particle, ∼15 to 20 km s^{-1} (Burchell et al., 2013) (the latter particles are in unbound orbits originating from interplanetary space, hence the higher mean speed). The speed and direction determination of time of flight (TOF) style detectors make them popular for application in space, with many TOF detectors previously used in space missions, including for example: the Cosmic Dust Detector (CDD) (Berg and Richardson, 1969) flown aboard the solar orbiters Pioneer 8 and 9, and deployed on the Moon in one of the Apollo 17 science experiments as the Lunar Ejecta and Meteorites (LEAM) instrument to detect meteorite and lunar ejeta impacts (Berg et al., 1973); the SPAce DUSt (SPADUS) instrument flown aboard the Earth orbiting Advanced Research and Global Observation Satellite (ARGOS) in low earth orbit (LEO) (Tuzzolino et al., 2001); the Cosmic Dust Analyzer (CDM) flown aboard the Cassini spacecraft to sample dust in interplanetary space and the Saturnian environment (Srama et al., 2004); the Piezoelectric Dust Detector (PDD) developed to fly on the 3U CubeSat ARMADILLO in LEO (Brumbaugh et al., 2012). The CDD and SPADUS detectors are based on thin films, with the basic principle being to determine the particle transit time between two films by measuring the physical phenomena produced in hypervelocity impacts with the films, the production of plasma, and depolarisation of the polyvinylidene fluoride (PVDF) film, respectively. Due to its relevance to this study, it is worth mentioning that PVDF has also been used in a considerable number of past single layer impact detectors in space missions, e.g. Vega to Halley's comet (Simpson et al., 1986), Stardust to comet Wild 2 (Tuzzolino et al., 2003), Cassini to Saturn (Srama et al., 2004), and the solar sail demonstrator the Interplanetary Kite-craft Accelerated by Radiation Of the Sun (IKAROS) (Hirai et al., 2014).

Subsequently, more research in the area of dust and debris detectors has led to various other TOF designs being developed by among others, NASA and JAXA (e.g.

Burchell et al. (2013), Nakamura et al. (2015), Liou et al. (2015), Hamilton et al. (2017), De Simone et al. (2019), Schimmerohn et al. (2021)). All of these designs feature either the use of polyimide films (12.5 μm thick) and/or acoustic detection of particle impacts to determine impactor speed. Thus a study of the accuracy and capabilities of detectors based on these features has value to this area of research. In particular, the Debris Resistive Acoustic Grid Orbital NASA-Navy Sensor (DRAGONS) developed by NASA'S Orbital Debris Programme Office (Liou et al., 2015; Hamilton et al., 2017; Anz-Meador et al., 2019) and an in situ debris measurement system being developed by JAXA (Nakamura et al., 2015), focus on the use of Kapton films as the detection surfaces. Kapton is a polyimide material that has excellent thermal properties (capable of withstanding both high and croyogenic temperatures), mechanical properties, and radiation resistance (Berkebile and Stevenson, 1981; Gouzman et al., 2019; Griseri, 2020). These properties make Kapton excellent for space based applications and it has been flown on spacecraft since the 1960's in a wide range of applications including; electrical wire insulation, photovoltaic modules, and most commonly spacecraft and instrument insulation (Berkebile and Stevenson, 1981; Henderson, 1989; Finckenor and Dooling, 1999; Smith et al., 2016). One drawback of its use in low Earth Orbit (LEO) is its susceptibility to atomic oxygen erosion (Banks, 1990). However, application of thin coatings of metals such as gold dramatically reduce this problem permitting the use of Kapton in LEO for prolonged periods. Therefore, its pedigree would suggest that it is an ideal material for use in TOF detectors. One crucial issue for such detectors is the accuracy with which they can measure the speed of incident particles. This paper presents results from a laboratory study on the speed determination capabilities and accuracy of Kapton based, acoustic TOF detectors.

2. Experimental method

A prototype TOF detector was constructed, comprising two Kapton films, each 12.5 μm thick (*f*), used as detection surfaces, mounted on aluminium frames with a separation (*x*) of 0.754 ± 0.001 m, see Fig. 1a. The surface of each film is 40 cm by 40 cm, comprising 1600 cm^2. Three polyvinylidene fluoride (PVDF) acoustic sensors were attached to identical positions on each film, labelled A & E, B & F, and C & G (Fig. 1b), with relative differences in location on the scale of the uncertainty in the measurement (0.001 m). This was achieved by manufacturing the prototype such that the frames were identical in size and directly in line with one another, thus the bottom left corner of each frame can be considered (0,0) of an x-y plane, with the second frame displaced along the z axis (along the LGG barrel axis) by *x*. Using this reference point it was possible to measure the location of the sensors by hand. These sensors are used to measure the time of impact. PVDF sensors were used as they are thin and flexible enough not to substan-
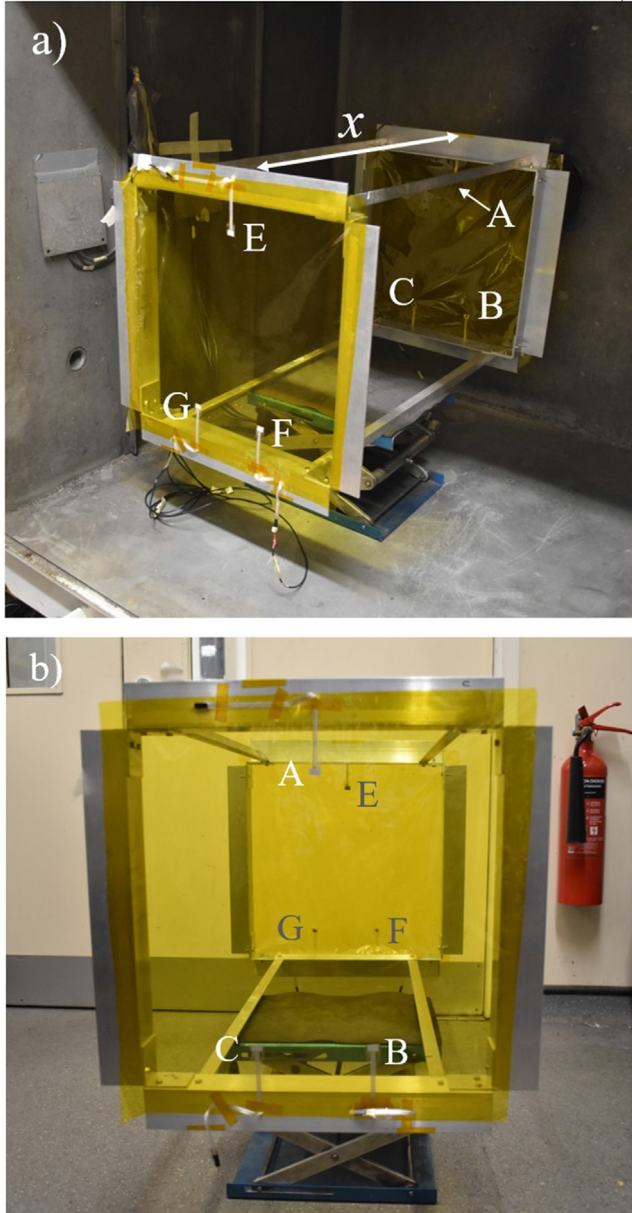
Fig. 1. (a) The prototype detector consisting of two Kapton layers (in yellow) mounted on square aluminium frames (each 40 cm by 40 cm) separated by horizontal aluminium struts, is shown positioned in the target chamber. The spacing between the two layers (x) is marked with an arrow. The projectile enters from the rear of the chamber at the far right, and proceeds at normal incidence through the two layers (moving towards the front left of the image). There are three PVDF sensors (each a white rectangular shape, with data read out via a long "tail" leading to the edge of the frame) on each Kapton layer. Sensors A, B and C are on the first layer as seen by the projectile (sensor A is obstructed by a strut and its location is marked by an arrow). Sensors E, F and G are on the second layer. (b) The detector as seen from the front. Sensors A, B, C (front face) are labelled in white text. Sensors E, F and G (grey text) are on the rear plane.

tially constrain the films, and have been shown to provide accurate timing measurements (e.g. Liou et al. (2006), Corsaro et al. (2016)), which can determine impact location with an average deviation of 0.8 cm (Hamilton et al., 2017).

In addition to their favourable mechanical properties, PVDF sensors do not require power (being piezoelectric), making them excellent for use in space applications, where power supply is limited. The prototype was mounted in the target chamber on a lab jack insulated with a rubber mat, which has been found to prevent transmission of any gun vibration in past experiments. Hypervelocity impact testing of the detector was carried out using the University of Kent's Light Gas Gun (LGG) (Hibbert et al., 2017). A significant feature of the LGG relevant to this study is its internal TOF speed chamber, positioned just before the target chamber. This chamber is equipped with two 3 mW lasers and optics that provide light curtains transverse to the projectile direction of flight. The lasers are 499 mm apart, and each is focused onto a fast photodiode. Interruption of the light by passage of the projectile alters the signal from the photodiode. Both photodiodes are read-out on a fast digital oscilloscope (50 MHz sampling). The relative timing of the interruptions to the two light signals, combined with their known separation, provides a projectile speed, v_{LGG}, to better than $\pm1\%$ (Burchell et al., 1999) for velocities up to 7 km s^{-1}. In this experiment 1 mm diameter, d_{pr}, stainless steel 420 (StSt420) spherical projectiles were accelerated to speeds of ~2 and 4 km s^{-1} at normal incidence to the detector, using a four-segment discardable split sabot propelled by nitrogen and helium gas, respectively. To suppress the low frequency vibrational modes that are not of interest here, a four-pole 15 kHz high-pass filter is applied in the PVDF preamplifier. The output voltages of the PVDF sensors were recorded using a standard laboratory PC running LabVIEW SignalExpress, taking 12000 samples recorded at a rate of 2.5 MHz and triggered by the impact of the discarded sabot on a stop plate located in the LGG blast tank. This recorded all of the required acoustic information with a precision of 0.4 μs.

3. Results

Seven hypervelocity impact experiments were carried out, with the incident projectile speed (v_{LGG}) shown in Table 1. To determine the speed of the projectile using the TOF method, the impact time on each film is required to calculate the time difference between impacts, Δt, and thus the time taken to traverse the separation x, which is equal to the flight path length. Using Eq. (1),

$$v = \frac{x}{\Delta t}, \tag{1}$$

the speed can be calculated directly from these quantities.

In each shot, three speeds were calculated, using the Δt from each pair of sensors. The signal arrival time from each sensor in a plane (A, B, C, and E, F and G) is different and is not the actual impact time on that plane, as it includes a time offset due to the transmission of the signal through the Kapton to the sensor. However, the pairs of sensors in the two planes (A & E, B & F, and C & G) are aligned behind

Table 1
Speed measurement results, showing speeds determined from pairs of sensors (v_{AE}, v_{BF}, v_{CG}), the average speed measured by the TOF detector (TOF Avg.), and the incident particle velocity as measured by the LGG's light gate system (v_{LGG}). The value marked with a ' * ' is an anomalous value, which is caused by a noise artefact present in the data. The value marked with a '**' is the average recalculated excluding the anomalous value.

Shot	v_{AE} (m s^{-1})	v_{BF} (m s^{-1})	v_{CG} (m s^{-1})	TOF Avg. (m s^{-1})	v_{LGG} ±1% (m s^{-1})	$\Delta_{TOF,LGG}$ (m s^{-1})
1	2081 ± 9	2084 ± 10	2085 ± 10	2083 ± 5	2084	1 ± 22
2	2191 ± 11	2192 ± 11	2210 ± 11	2198 ± 6	2192	6 ± 22
3	2124 ± 10	2125 ± 10	2174 ± 10	2141 ± 6	2132	9 ± 22
4	3937 ± 33	4470 ± 43*	3872 ± 32	4093 ± 21	3900	193 ± 44
				3905 ± 23**		5 ± 45**
5	3770 ± 33	3780 ± 30	3802 ± 31	3784 ± 18	3779	5 ± 42
6	3740 ± 27	3720 ± 30	3783 ± 31	3748 ± 17	3740	8 ± 41
7	2083 ± 13	2073 ± 13	2094 ± 13	2084 ± 8	2097	13 ± 22

each other in the direction of flight, so the transit times should be similar and the time difference between a pair should be equal to the transit time of the projectile between the two planes. The three individual estimates of the projectile transit time in a shot are then combined with the known separation x to provide three separate measurements of the speed of the projectile between the two planes (v_{AE}, v_{BF}, and v_{CG}). These three values are then averaged (TOF Avg.) which can be compared to the speed measured upstream in the gun itself (v_{LGG},) and the difference determined ($\Delta_{TOF,LGG}$). All values are presented in Table 1 (the associated uncertainties are discussed below).

The arrival time of the signal at each sensor was taken as the onset time of the largest peak to peak (P-P) amplitude, in the first set of peaks. The first largest P-P amplitude was used as it provides a systematic approach to onset determination. Similarly, it is the most easily identified point in each trace, and it is assumed that this component of the acoustic signal would arrive at each of the sensors at the same relative time. Time of onset was identified by finding the two adjacent peaks and troughs (or vice versa) with the largest P-P amplitude and then following the trace back to where this peak to peak oscillation began and taking the time of onset as the first recorded data point on the slope, above the noise level. This data point typically had a magnitude of 0.03 V from the zero point, while the electronic noise in the data acquisition system had a P-P amplitude of 0.005 V. The first largest P-P amplitude, was used as comparable or larger peaks later in time could be due to reflections and/or the superposition of waves, thus not being representative of the largest signal from the impact. A typical set of signals is shown in Fig. 2. Note that it was the relative magnitude of peaks in a given trace, e.g. A, that were considered to determine the largest peak size, due to these signals being raw data and thus not normalised to account for the loss of signal intensity due to signal spreading and attenuation in the Kapton film. Fig. 2 shows a good example of this; here the impact occurred 31 ± 1 mm from sensor A, 280 ± 1 mm from B, and 276 ± 1 mm from C, and it is clear to see that the magnitude of the P-P amplitude for B and C is $\frac{1}{5}$ the magnitude recorded by A. Furthermore, only signal timing is of importance to this study and this would always depend on the relative magnitude of signals in a given trace.
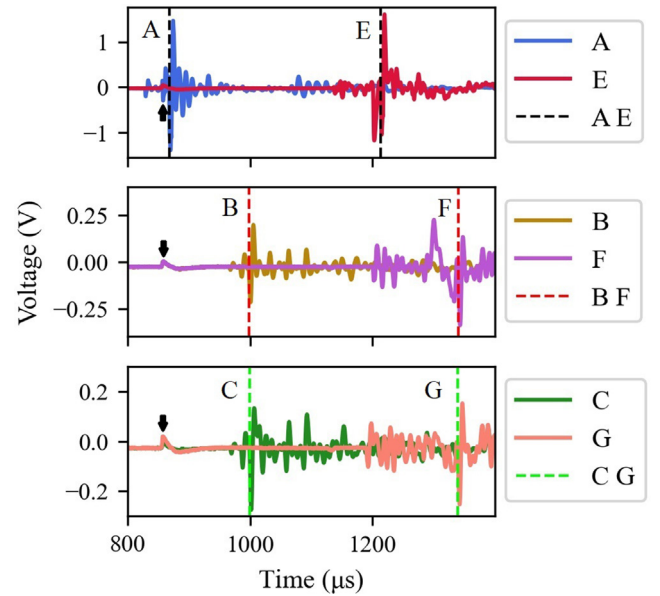

Fig. 2. The key time period of a typical set of acoustic signals in an impact (Shot 2 in Table 1) from each sensor, shown in pairs. Dashed vertical lines represent the onset time for each sensor, with each onset time corresponding to each sensor labelled for clarity. Small noise signals can be seen in signals B, C, E, F and G, marked with black arrows.

The uncertainty in the onset time for each sensor, δt, was taken as $\delta t = 1$ μs, a little over twice the sampling precision. This helps account for the variation in signal shape that causes signal onset times for sharp well-defined peaks with no noise to be determined more accurately than for broad and/or noisy peaks. The resulting errors in the transit times are combined with the uncertainty in the separation of the two planes of Kapton to yield the uncertainty in the derived speed. Averaging the speed over all three pairs of sensors was employed to further reduce these errors. The uncertainty arising from signal peak shape is indicated by the results for Shot 3 v_{CG} and Shot 4 v_{BF}. Clearer peaks such as those corresponding to A & E and B & F in Shot 3 (see Fig. 3) gave velocities separated by only 1 m s^{-1} and much closer to v_{LGG} than for the value calculated from C & G, which had a larger absolute deviation from v_{LGG}. Data from Shots 1, 5, and 6 can also be seen in Figs. 4–6, respectively further showing the variability in signal shape between shots.
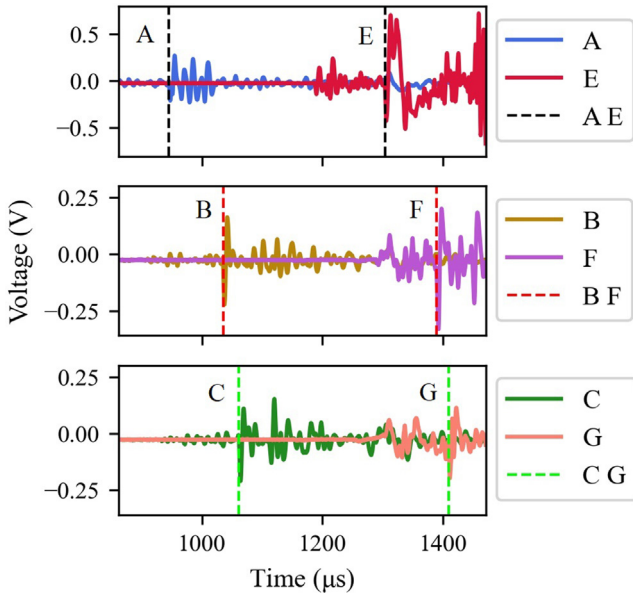
Fig. 3. The region of interest of acoustic signals for Shot 3 in Tables 1 and 2. The sharper the start of the signal, the more accurate the determination of the start time. Sensors A and E have sharp rise times, as do B and F. However, the start of C and particularly G is less well determined leading to a greater inaccuracy in the estimate of the flight speed based on sensors C and G.
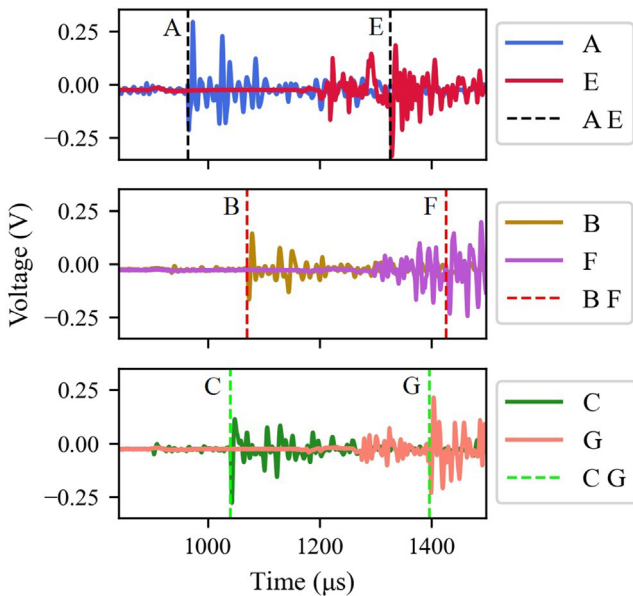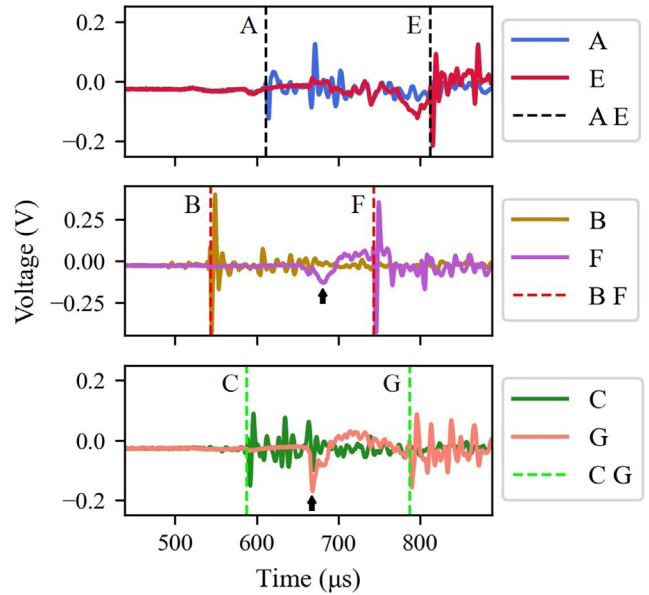

Fig. 5. The key time period of acoustic information in Shot 5, which includes noise in the traces of F and G, marked with black arrows, and similarly a small noise peak in E leading to a downward slope before the acoustic information from the impact arrives. This noise did not significantly effect the determination of the time of impact.

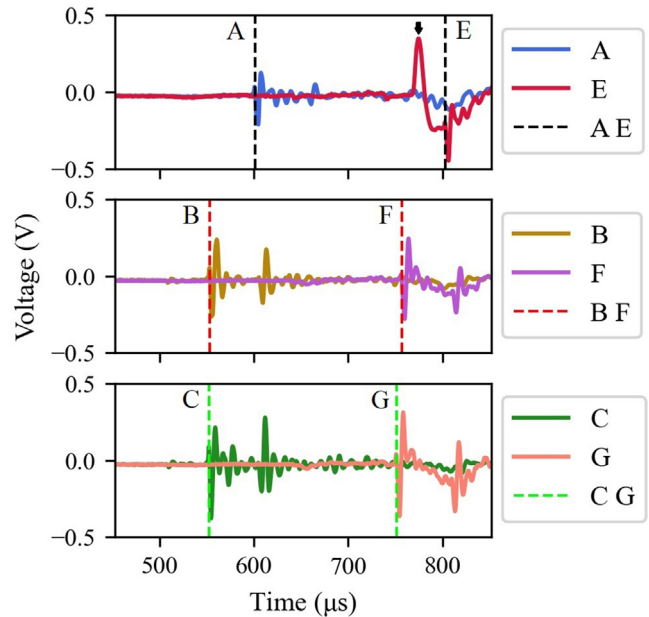Fig. 4. The key time period of acoustic information in Shot 1.

Fig. 6. The key time period of acoustic information in Shot 6. Sensor E shows a non-acoustic single noise peak with a small recover tail, marked with a black arrow, before the oscillatory acoustic waves arrive. This noise did not significantly effect the determination of the time of impact.

Shot 4 v_{BF} (see Fig. 7) is an anomalous value caused by non-acoustic noise in the signal making onset determination inaccurate. This non-acoustic noise may originate from photons, and/or electrons and ions produced in the plasma created in impacts. The variability of induced plasma and light flash between shots is complicated, as is the PVDF sensor response, and both of these aspects are under further investigation in a separate programme.

Non-acoustic noise can be distinguished from the data due to its difference in profile. The acoustic data of interest, exemplified in the aforementioned figures, has a negative-positive, or vice versa, oscillatory form, characteristic of the oscillations associated with the acoustic waves that decay with time. In Fig. 7 we see the non-acoustic noise
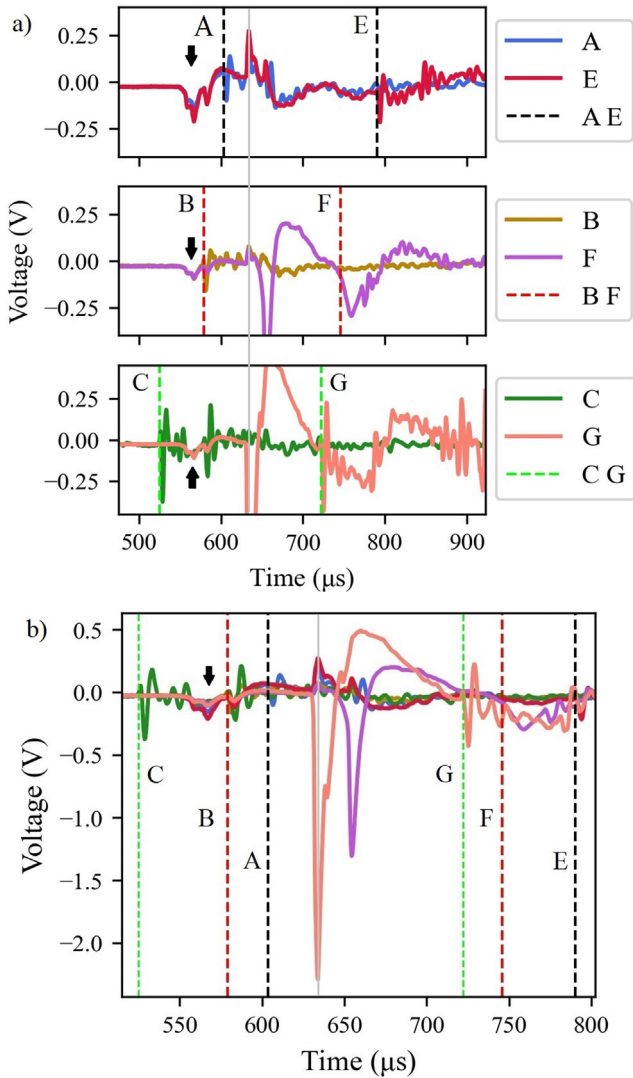
Fig. 7. (a) The key time period of acoustic information in Shot 4 showing the noise artefacts contaminating this data set, shown occurring centrally. The large non-oscillatory peaks in G and F are characteristic of non-acoustic noise, as well as signals occurring across multiple sensors, even on different films, at the same time, A, E, and G, as illustrated by the light grey solid vertical line at 634 μs. Black arrows mark small non-acoustic noise peaks which did not effect signal onset determination. (b) Roughly the same time period as in (a) only with all trace shown on the same plot and the y-axis extended to show the full magnitude of the noise peaks.

artefacts that lead to the anomalous result in Table 1 and 2. Unlike the oscillatory acoustic waves these are relatively large, broad, single peaks followed by a recovery tail, which contaminates the onset of signal F.

Other features characteristic of noise include: almost identical signals detected by different sensors (which is unexpected due to, for example, propagation effects which result in differences in the observed signals), and signals occurring across different spatial locations at the same time. Fig. 7 shows both of these features with E and A (sensors on different films) showing almost identical signals at the exact same time as the non-acoustic noise in signal G, illustrated by the light grey solid vertical line, further con-

firming this as a non-acoustic signal. Fig. 2, 5, and 7 also show smaller non-acoustic noise features consisting of a broader than expected single peak with a recover tail occurring at the same time, marked with black arrows. Data from Shot 6 also shows a non-acoustic noise feature in signal trace E, again a single peak with a small recovery tail, Fig. 6.

Another source of noise are the small oscillatory peaks which precede the acoustic data of interest in traces A, B, and C, these can be seen in Fig. 3–6. These small peaks are thought to be longitudinal acoustic waves from the impact, which arrive before the shear waves (transverse waves) of interest (the shear waves are of interest here since they are of larger magnitude, making them easier to identify, and because the precursor longitudinal waves are not always detected, see traces A, F and G in Fig. 6. To confirm that the relatively large peaks observed in the second film, immediately preceding the largest peak which is taken as the signal, are not an artifact of acoustic waves transmitted through the prototype structure, tap tests, and a shot with separate isolated films (Shot 7 in Tables 1 and 2) were carried out. The tap tests involved striking the layers with short sharp taps, and whilst signals could be observed in sensors on the same layer as the tap, none were observed in the other layer, indicating no transmission of signals between layers. The experimental set up in Shot 7 was different to that of the other shots, in that the individual Kapton film layers were no longer connected by a common frame. They were still positioned parallel to each other, 750 ± 2 mm apart and orthogonal to the direction of projectile flight, but stood on separate insulated mounting platforms. The projectile and readout of the sensors were the same as for shots 1–6, with the projectile speed given in Table 1. The signals from the PVDF sensors (Fig. 8) showed many features in common with the other shots, in particular, they displayed the signals on the second layer that immediately precede the largest amplitude signal. This occurs, despite the absence of a connecting frame, indicating that transmission through the frame is not responsible.

It could be supposed that the preceding peaks are due to co-moving gas accompanying the projectile after its release from the sabot. To test this, an experiment with an empty sabot was carried out; all experimental parameters were kept consistent with the 1 mm StSt420 spherical projectile shots at 2 km s^{-1}, except the sabot had no projectile loaded. Thus when fired, the only thing to continue through the stop plate and into the target chamber would have been the co-moving gas accelerated in front of and around the sabot, followed by later arriving gunpowder, soot and possible debris from the first stage of the gun. In this shot, only powder and soot hit the first film with no noticeable debris coming down and nothing penetrating the first film. The sabot attained a speed of 2176 m s^{-1} $\pm 4\%$ (the larger uncertainty is due to using the muzzle laser and stop plate impact for timing instead of the light curtain system) and the data corresponding to this shot is shown in Fig. 9.

Table 2
Results for the wave speed in the Kapton film as calculated from the difference in path lengths and travel times for sensors on the same film. WS$_{AB}$ corresponds to the wave speed calculated from the differences between sensors A & B, etc. WS is the average of all WS$_{nn}$ values from each shot. The onset times that determined the difference in travel time are the same as those used in calculations for Table 1. The separately measured value for the wave speed is 1875 ± 25 m s^{-1}. The value marked with a ' * ' is an anomalous value, which is caused by a noise artefact present in the data. The value marked with a '**' is the average recalculated excluding the anomalous value.

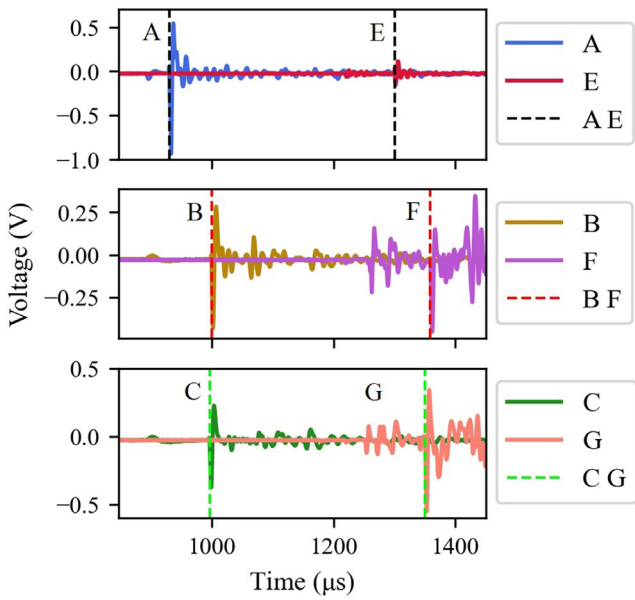| Shot	WS$_{AB}$ (m s^{-1})	WS$_{AC}$ (m s^{-1})	WS$_{EF}$ (m s^{-1})	WS$_{EG}$ (m s^{-1})	WS (m s^{-1})
1	1917 ± 29	1868 ± 39	1930 ± 31	1889 ± 42	1901 ± 18
2	1913 ± 23	1873 ± 23	1916 ± 24	1917 ± 24	1904 ± 12
3	1875 ± 33	1828 ± 25	1879 ± 35	1967 ± 29	1887 ± 16
4	1694 ± 112	1860 ± 38	803 ± 41*	1947 ± 46	1576 ± 33
					1833 ± 42**
5	1938 ± 46	2044 ± 140	1922 ± 44	1905 ± 121	1952 ± 49
6	1852 ± 62	1996 ± 65	1894 ± 66	1907 ± 59	1911 ± 32
7	1921 ± 44	1864 ± 45	1879 ± 52	1941 ± 62	1901 ± 26

Fig. 8. The key time period of acoustic information in Shot 7. In this shot the two film layers did not have a connecting structure, yet the signals on the second film are similar to those where the connecting frame was used, indicating that transmission via a frame is not the cause.
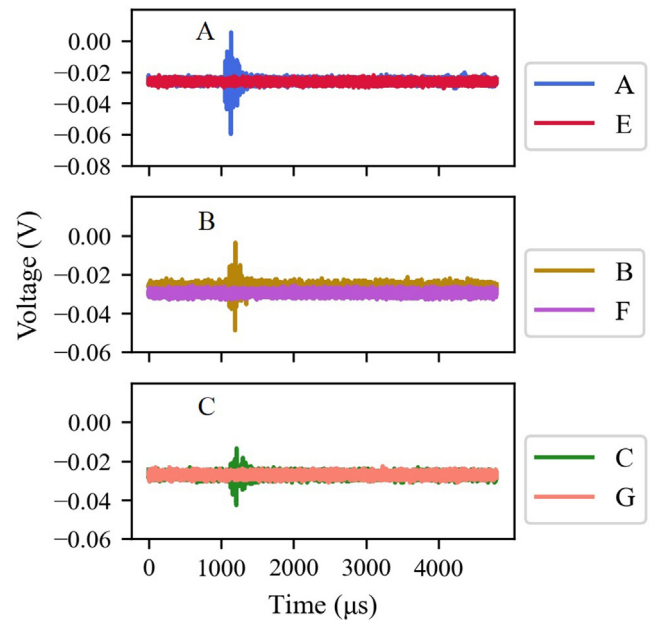

Fig. 9. The full traces of the acoustic data recorded for the empty sabot shot, showing only one set of peaks of low magnitude. These were on the first film only (sensors A, B, and C), and were well after the expected arrival time predicted from the sabot speed. These signals likely correspond to the deposition of slower moving powder and soot.

Only one set of peaks are observed in the data in Fig. 9, which correspond to the powder and soot hitting the film. Considering the onset time of these peaks, the data arrives later in time than would be expected for a projectile or preceding gas blast, confirming that these arise from later powder deposition and can not be mistaken for a projectile. This suggests that there are no signals produced by co-moving gas. No signals being detected in the second film further confirms that no gun vibration is transmitted through the insulated mounting, and similarly that no acoustic signals from the impact on the first film are transmitted through the detector structure to the second film.

In cases where the flight path of the projectile was not perfectly normal to the detector, due to, for example, being pushed slightly off axis by the sabot as it separated, slight ~mm deviations from the first impact location were recorded on the second film, as measured by hand. Such

a small deviation from the flight path would have a negligible effect on x, a 5 mm difference in location corresponding to ~0.01 mm difference in x, far smaller than the uncertainty for this value. However, the relative difference to the acoustic wave travel time through the Kapton in a plane to the various sensors would be relatively larger, with 5 mm representing a 14% difference for a sensor to impact distance of 35 mm. For these cases a correction to Δt was made to account for the differences in travel times for the acoustic waves in the Kapton film. These corrections were calculated from the mm scale difference in wave path lengths using the wave speed in 12.5 μm Kapton film, $v_{wave} = 1875 \pm 25$ m s^{-1}, previously determined at Kent in unpublished data. This known wave speed also allows for an independent verification of the accuracy of the time of impact measurements. By comparing the time of impact
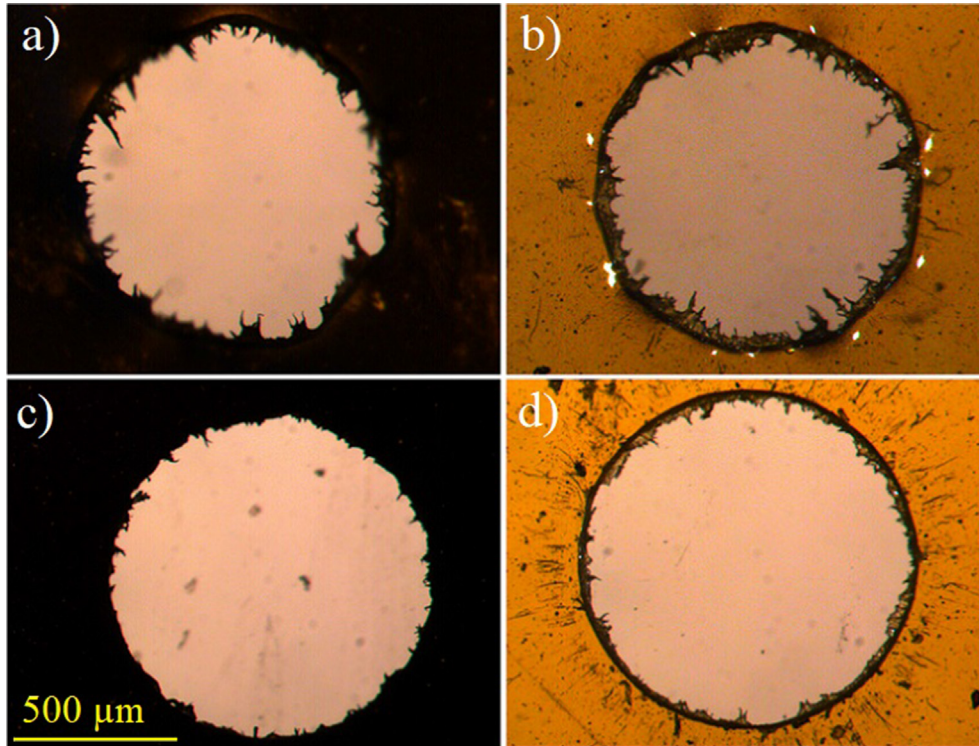
Fig. 10. Optical images of penetration holes viewed from the incident direction of the 1 mm stainless steel projectiles. (a & b) Holes in the 1st and 2nd films have diameters of 1000 ± 8 μm and 1003 ± 8 μm respectively, after impact at $\sim$2 km s^{-1} (Shot 2). (c & d) Holes in the 1st and 2nd films have diameters of 1010 ± 12 μm and 1037 ± 8 μm respectively, after impact at $\sim$4 km s^{-1}(Shot 5). The first films are blackened by the deposition of gunpowder/soot generated by the first stage of the gun.

between sensors on the same film, e.g. A & B, and A & C, and the difference in wave path lengths for each sensor, the wave speed can be directly calculated from the experimental data. Thus, it can be considered that time of impacts which return a wave speed of 1875 m s^{-1}, within uncertainties, represent the same relative time of impact agreed by multiple sensors, and represent an accurate measure of the onset time. Accordingly, Table 2 shows the wave speeds calculated from the difference in travel times between sensors on each film, with WS$_{AB}$ corresponding to the wave speed calculated from the difference between A & B, etc. In Shot 3, the larger inaccuracy in the start time of the signals from sensors C and G, has resulted in an absolute value for the wave speed which deviates from the previously measured value in the Kapton film, more than other sensor combinations. The anomalous result produced by noise contamination can also be identified from this validation method. Shot 4 WS$_{EF}$ shows a significantly different value from the measured wave speed, and a value for WS$_{EG}$ all but within uncertainties, suggesting that E and G are well determined while F has not been determined accurately. Further to this WS$_{AB}$ has a small deviation from the measured value suggesting that signal B may give a less accurate onset time, the combination of B and F would then lead to the anomalous result observed.

Previous work on the passage of projectiles through thin films has suggested that at speeds in excess of a few km s^{-1},

the ratio of film thickness to projectile diameter ($f : d_{pr}$) is critical in determining if the projectile undergoes disruption in the impact process (e.g. Gardner et al. (1997)). For the projectiles here, with a film thickness to projectile diameter ratio $f : d_{pr} = \frac{1}{80}$, no disruption of the projectile is expected. Inspection of the penetration holes in the Kapton films used in the detector showed similar penetrations on both films (Fig. 10) confirming that the projectiles were not appreciably disrupted.

During penetration the projectiles melted the Kapton films, producing melted and charred Kapton around the circumference of the holes (see rough edges of penetration holes in Fig. 10). As the projectile speed increases, the pressure and friction induced during impact also increases causing a larger amount of the Kapton to vaporize and melt as evident from there being fewer and smaller filaments of melted Kapton present in Fig. 10c and d than in a and b. A view from the back of the 2nd film in Shot 5 shows that at higher speeds more of the Kapton is melted and removed from the penetration hole, removing the filaments, and thrown in such a way as to deposit it on the back of the film (seen as black lines radiating from the penetration hole in Fig. 11).

At both speeds, penetration holes in the first film had diameters, given in Fig. 10, that are equal to d_{pr}. This confirms that for Kapton a ratio of $f : d_{pr} = \frac{1}{80}$ leads to a penetration hole diameter, d_h, equal to that of the projectile
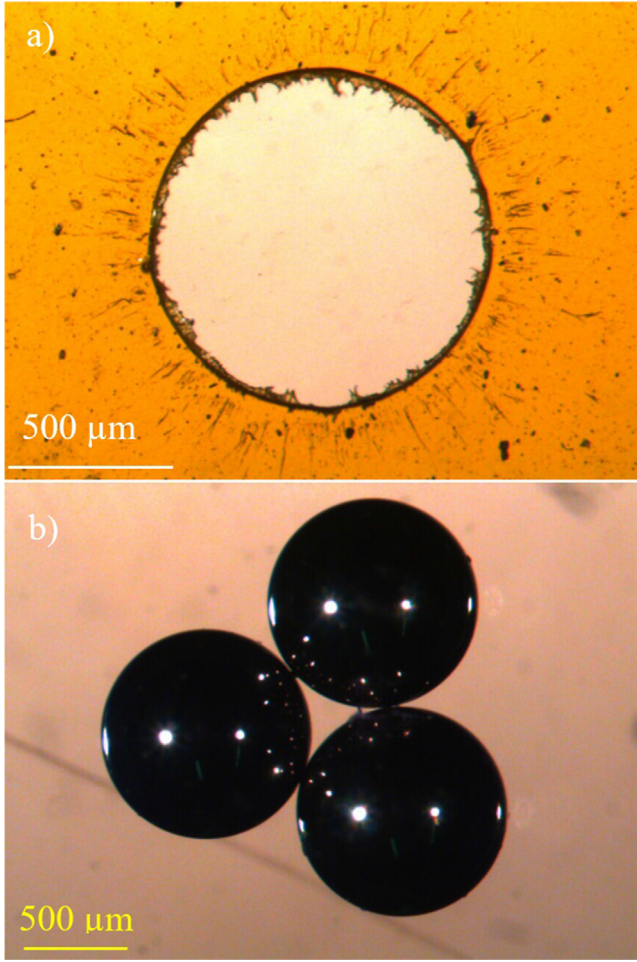
Fig. 11. (a) Penetration hole, viewed from the rear, in the second film after penetration of a 1 mm stainless steel projectile traveling at ~4 km s^{-1}, (Shot 5). (b) Typical examples of how spherical and accurate to 1 mm the diameters of the 1 mm stainless steel projectiles are. Three randomly selected spheres from the 1 mm stainless steel supply were all 1000 ± 8 μm.

($d_h = d_{pr}$), which represents the ultra-thin film limit (Hörz, 2012). d_h for the penetrations at ~4 km s^{-1} in the second film were larger than for 2 km s^{-1}. The larger $d_h = 1037 \pm 8$ μm in the second film could be indicative of more Kapton from the first film being accumulated on the projectile, increasing its effective diameter. This would be characteristic of the higher temperatures involved producing more melted Kapton. All three shots at each speed, gave similar results for d_h in the respective film layer to the examples shown in Fig. 10, with the 4 km s^{-1} impacts producing larger diameters in the second film than the first (1028 ± 8 μm and 1033 ± 8 μm for the 3.90 and 3.74 km s^{-1} impacts respectively).

4. Discussion

There have been previous studies on hypervelocity impacts into Kapton films, e.g. Neish et al. (1997) and Nakamura et al. (2015), however these were at smaller particle sizes; 57 μm to 400 μm ($f : d_{pr} = \frac{175}{57}$ to $\frac{1}{16}$) and 50 μm to 516 μm ($f : d_{pr} = \frac{1}{4}$ to $\frac{25}{1032}$), respectively. These studies lack any treatment and discussion of the deceleration of projectiles penetrating the Kapton films. Similarly, there is previous work in the literature that concerns larger projectiles, similar to those used in this study (~ mm), penetrating thin films (e.g. Hörz et al. (1994), Gwynn et al. (1997), Hörz (2012)). Again these studies do not investigate or discuss the speed of the projectiles post penetration. Previous work on the deceleration of a projectile due to the penetration of thin films is summarised in Table 3. The data in Table 3 reported that no deceleration was observed for the values of $f : d_{pr}$ considered here; however the previous work was all at significantly smaller absolute size scales. The current study herein, has significantly increased the absolute parti-

Table 3
A comparison of the lack of deceleration for 1 mm stainless steel 420 (StSt420) projectiles penetrating Kapton films in this study, with the results of other projectile-film combinations in previous works. d_{pr}, f, and v_{in} stand for projectile diameter, target film thickness, and incident velocity, respectively.

Impact speed (km s^{-1})	Projectile: Target composition	d_{pr} (μm)	f (μm)	$f : d_{pr}$	$\frac{\Delta v}{v_{in}}$	Reference
2 & 4	StSt420: Kapton	1000	12.5	0.013	<1%	This work
1–5	Iron: Cellulose	0.6–3	0.07	0.02–0.12	<2%	(Burchell et al., 1998)
2.5–7.5	Glass: PVDF	52–85	28	0.3–0.5	~20%	(Simpson and Tuzzolino, 1989)
4.3–11	+ 120 nm Al	41–71	6	0.08–0.15	<5%	
2.5	Fe: Mylar	2.3	2.4	1.04	13%	(Capaccioni and McDonnell, 1986)
3	Fe	1.3	0.3 Parylene	0.3	4%	(Pailer and Grün, 1980)
	Al	1.9	+ 0.075 Al	0.2	8%	
	Glass	2.0		0.19	9%	
	Polyphenylene	2.4		0.16	14%	
2–12	Fe: Al	0.6–3	0.2–0.8	0.07–1.3	5–30%	(Grün and Rauser, 1969)
	Au	0.6–3	0.1–0.6	-	-	
	Carbon	0.6–3	0.1	0.03–0.17	<2%	
	Nitrocellulose	0.6–3	0.05	0.017–0.08	<2%	
2–10	Fe: 0.42 μm Parylene + 0.1 μm Cu + 0.06 μm Al	0.3–6	0.58	0.10–1.93	5–40%	(Berg and Richardson, 1969)

cle size to mm sized particles (similar to the debris size of interest in LEO) and used corresponding thicker films. Extending the the projectile size, to mm sized, for penetrations into Kapton films also confirms that an impact damage equation for Kapton would need to attain $d_h = d_{pr}$ at or before $d_h/f = 80$, a useful addition to the data used to derive the impact damage equation for Kapton presented by Neish and Kibe (2001).

With the TOF detector measuring the same velocity as the LGG's light-gate system within 0.5%, a value smaller than the combined uncertainty of $\sim1\%$, no deceleration was detected. Hence, the TOF system provides an accurate measure of the speed of mm sized particles. This current work is, however, for mm sized impactors. This agrees well with the size regime of orbital debris which pose a significant threat to spacecraft. There are, however, other considerations to be allowed for. The first is a fuller speed range. Orbital debris can impact at greater speeds than used here, as will natural cosmic dust, which on average travels at twice the speed of debris. When scaling the same precision-based uncertainties to velocities of 10 km s^{-1} the uncertainty in v increases to 2%. However, for space implementation a larger sampling frequency of 5 MHz and or a more accurate determination of x would lead to uncertainties approaching $\sim1\%$. Thus the system would still provide accurate estimates of the impact speed. Another complication lies in the shape of the debris and its strength. Here a spherical stainless steel projectile was used. However, the DebrisSat experiments (Cowardin et al., 2019), have indicated that there are five main shapes for debris arising from satellite fragmentation, including fragile thin (paint) flakes. The behaviour of the latter in particular, on penetrating the front film would need to be established in future work (e.g. will they break up?). Also, even for spherical projectiles, as the ratio of $f : d_{pr}$ increases, the work of Gardner et al. (1997) shows that the penetration process changes. At some value of this ratio, the interaction with the film will appreciably slow the projectile (Table 3), and this may occur before the onset of projectile disruption. Table 3 shows that deceleration varies with film material and as such it is important to calibrate individual films and detectors for the detection of particles with larger $f : d_{pr}$, and this will be the subject of future work.

5. Conclusion

The successful application of TOF detector systems as orbital debris monitors relies on various properties, including their ability to accurately determine the impact speed. Here it has been shown that under ideal conditions, this can be done to better than 1% accuracy for Kapton based, acoustic TOF detectors. It is shown that 1 mm stainless steel spheres traveling at speeds of ~ 2 and 4 km s^{-1} do not experience significant disruption or deceleration during their passage through 12.5 ± 0.2 μm Kapton films. Further

still, penetration holes for projectiles much larger than the thickness of Kapton film, $d_{pr} \gg f$, tend towards the ultra-thin film limit of $d_h = d_{pr}$. More work remains to extend this result to different impactor types and sizes, and to determine and calibrate velocity loss for smaller particles, among other objectives, but the general applicability of the method is demonstrated making such detectors ideal for space applications. For a real detector deployed in space, which will experience non-normal impacts, the actual resolution of both impact speed and direction will depend on the accuracy of the determination of the impact location on the films, which would be specific to the particular detector.

Declaration of Competing Interest

The authors declare that they have no known competing financial interests or personal relationships that could have appeared to influence the work reported in this paper.

References

Anz-Meador, P., Ward, M., Manis, A., Nornoo, K., Dolan, B., Claunch, C., Rivera, J., 2019. The Space Debris Sensor Experiment. Presented at the First International Orbital Debris Conference, Texas (USA). 10 pages. URL: https://ntrs.nasa.gov/citations/20190033909.

Banks, B., 1990. Atomic oxygen interaction with materials on LDEF. In: Stain, B.A., Young P.R., (Eds.), In Proc. LDEF Materials Data Analysis Workshop. pp. 191–216. NASA Conference Publication 10046.

Berg, O.E., Richardson, F.F., 1969. The pioneer 8 cosmic dust experiment. Rev. Sci. Instrum. 40, 1333–1337. https://doi.org/10.1063/1.1683778.

Berg, O.E., Richardson, F.F., Burton, H., 1973. Lunar Ejecta and Meteorites Experiment, NASA SP-33, 16–1 – 16–9.

Berkebile, D.H., Stevenson, D.L., 1981. The use of kapton polyimide film in aerospace applications. SAE Technical Papers 90, 3562–3568. https://doi.org/10.4271/811091.

Brumbaugh, K.M., Kjellberg, H.C., Glenn Lightsey, E., Wolf, A., Laufer, R., 2012. In-situ sub-millimeter space debris detection using cubesats. Adv. Astronaut. Sci. 144, 789–803.

Burchell, M.J., Cole, M.J., McDonnell, J.A., 1998. Role of particle charge in impact ionization by charged microparticles. Nucl. Instrum. Methods Phys. Res., Section B: Beam Interact. Mater. Atoms 143, 311–318. https://doi.org/10.1016/S0168-583X(98)00371-1.

Burchell, M.J., Cole, M.J., McDonnell, J.A.M., Zarnecki, J.C., 1999. Hypervelocity impact studies using the 2 MV Van de Graaff accelerator and two-stage light gas gun of the University of Kent at Canterbury. Measurm. Sci. Technol. 10, 41–50.

Burchell, M.J., Corsaro, R., Giovane, F., Cole, M., Sadilek, A., Price, M.C., Liou, J.C., 2013. A new cosmic dust detector with a novel method using a resistive grid sensitive to hypervelocity impacts. Procedia Eng. 58, 68–76. https://doi.org/10.1016/j.proeng.2013.05.010.

Capaccioni, F., McDonnell, J.A., 1986. Experimental measurement of particle deceleration and survival in multiple thin foil targets. Adv. Space Res. 6, 17–20. https://doi.org/10.1016/0273-1177(86)90205-X.

Corsaro, R.D., Giovane, F., Liou, J.-C., Burchell, M.J., Cole, M.J., Williams, E.G., Lagakos, N., Sadilek, A., Anderson, C.R., 2016. Characterization of space dust using acoustic impact detection. J. Acoust. Soc. Am. 140, 1429–1438. https://doi.org/10.1121/1.4960782.

Cowardin, H., Anz-Meador, P., Murray, J., Liou, J.-C., Christiansen, E., Sorge, M., Fitz-Coy, N., Huynh, T., 2019. Updates to the DebriSat Project in Support of Improving Breakup Models and Orbital Debris Risk Assessments. In: Proceedings of the 2019 15th Hypervelocity Impact Symposium. https://doi.org/10.1115/HVIS2019-066.

De Simone, M.E., Andreades, C., Meo, M., Ciampa, F., 2019. Smart composite detector of orbital debris and micrometeoroids particles. Mater. Today: Proc. 34, 202–209. https://doi.org/10.1016/j.matpr.2020.02.796.

Dorschner, J., 2001. Interstellar dust and circumstellar dust disks. In: Grün, E., Gustafson, B., Dermott, S., Fechtig, H. (Eds.), Interplanetary Dust. Springer, pp. 727–786.

Draine, B.T., 2003. Interstellar Dust Grains. Ann. Rev. Astron. Astrophys. 41, 241–289. https://doi.org/10.1146/annurev.astro.41.011802.094840, arXiv:0304489.

Finckenor, M. M., Dooling, D., 1999. Multilayer Insulation Material Guidelines. Pub. NASA (Marshall Spacefligth Centre) NASA/TP/-1999-209263I. URL: https://ntrs.nasa.gov/api/citations/19990047691/downloads/19990047691.pdf.

Gardner, D.J., McDonnell, J.A., Collier, I., 1997. Hole growth characterisation for hypervelocity impacts in thin targets. Int. J. Impact Eng 19, 589–602. https://doi.org/10.1016/s0734-743x(96)00047-4.

Gouzman, I., Grossman, E., Verker, R., Atar, N., Bolker, A., Eliaz, N., 2019. Advances in Polyimide-Based Materials for Space Applications. Adv. Mater. 31, 1–15. https://doi.org/10.1002/adma.201807738.

Griseri, V., 2020. Polyimide used in space applications. In: Diaham, S. (Ed.), Polyimide for Electronic and Electrical Engineering Applications, chapter 5. (pp. 1–19). Pub. IntechOpen. URL: https://doi.org/10.5772/intechopen.93254.

Grün, E., Gustafson, B.A. S., Dermott, S., Fechtig, H., (Eds.), 2001. Interplanetary Dust. Pub. Springer, pp. 804.

Grün, E., Krüger, H., Srama, R., 2019. The Dawn of Dust Astronomy. Space Sci. Rev. 215. https://doi.org/10.1007/s11214-019-0610-1.

Grün, E., Rauser, P., 1969. Penetration Studies of Iron Dust Particles in Thin Foils. Space Research 9, 147–154.

Gwynn, D.W., Horz, F., Bernhard, R.P., See, T.H., 1997. The Dispersion of Molten Soda-Lime Glass Projectiles Following Penetration of Thin Aluminum Membranes. Int. J. Impact Engng. 20, 325–336.

Hamilton, J., Liou, J.-C., Anz-Meador, P., Corsaro, B., Giovane, F., Matney, M., Christiansen, E., 2017. Development of The Space Debris Sensor. In: Schmitz, T., Flohrer, F. (Eds.), Proceedings of the 7th European Conference on Space Debris. Pub. ESA Space Debris Office, 11 Pages. URL: https://conference.sdo.esoc.esa.int/proceedings/sdc7/paper/965.

Henderson, R.A., 1989. Thermal Control of Spacecraft. In: Fortescue, P., Stark, J. (Eds.), Spacecraft Systems Engineering (2nd ed.), chapter 12. Pub. John Wiley & Sons. England. pp. 337–364.

Hibbert, R., Cole, M.J., Price, M.C., Burchell, M.J., 2017. The Hypervelocity Impact Facility at the University of Kent: Recent Upgrades and Specialized Capabilities. Procedia Eng. 204, 208–214. https://doi.org/10.1016/j.proeng.2017.09.775.

Hirai, T., Cole, M.J., Fujii, M., Hasegawa, S., Iwai, T., Kobayashi, M., Srama, R., Yano, H., 2014. Microparticle impact calibration of the Arrayed Large-Area Dust Detectors in INterplanetary space (ALADDIN) onboard the solar power sail demonstrator IKAROS. Planet. Space Sci. 100, 87–97. https://doi.org/10.1016/j.pss.2014.05.009.

Hörz, F., 2012. Cratering and penetration experiments in aluminum and teflon: Implications for space-exposed surfaces. Meteorit. Planet. Sci. 47, 763–797. https://doi.org/10.1111/j.1945-5100.2012.01354.x.

Hörz, F., Cintala, M., Bernhard, R.P., See, T.H., 1994. Dimensionality scaled penetration experiments: Aluminum targets and glass projectiles 50 μm to 3.2 MM in diameter. Int. J. Impact Eng 15, 257–280. https://doi.org/10.1016/S0734-743X(05)80017-X.

Kessler, D.J., Reynolds, R.C., Anz-Meador, P.D., 1989. Orbital Debris Environment for Spacecraft Designed to Operate in Low Earth Orbit. Pub. Report Johnson Space Center Houston, USA, NASA Technical Memorandum 100 471, 22 pages.

Liou, J., Giovane, F.J., Corsaro, R.D., Burchell, M.J., Drolshagen, G., Kawai, H., Stansbery, E.G., Tabata, M., Westphal, A.J., Yano, H., 2006. LAD-C: A large area debris collector on the ISS. Presented at the 36th Scientific Assembly of COSPAR, Beijing (China). 7 pages. URL: https://ntrs.nasa.gov/api/citations/20060028448/downloads/20060028448.pdf.

Liou, J.C., 2006. Risks in Space from orbiting Debris. Science 311, 340–341. https://doi.org/10.1016/j.asr.2005.06.021.

Liou, J.-C., Corsaro, R., Giovane, F., Anderson, C., Sadilek, A., Burchell, M., Hamilton, J., 2015. DRAGONS – A Micrometeoroid and Orbital Debris Impact Sensor. Presented at the Nano-Satellite Symposium, Kobe-Hyogo (Japan). 6 pages. URL: https://ntrs.nasa.gov/archive/nasa/casi.ntrs.nasa.gov/20150019424.pdf.

Nakamura, M., Kitazawa, Y., Matsumoto, H., Okudaira, O., Hanada, T., Sakurai, A., Funakoshi, K., Yasaka, T., Hasegawa, S., Kobayashi, M., 2015. Development of in-situ micro-debris measurement system. Adv. Space Res. 56, 436–448. https://doi.org/10.1016/j.asr.2015.04.009.

NASA, 2020. Orbital Debris Quarterly News,. 24, 1–14. Pub. NASA, Orbital Debris Program Office, Houston (USA).

NASA, 2021a. Orbital Debris Quarterly News,. 25, 1–12. Pub. NASA, Orbital Debris Program Office, Houston (USA).

NASA, 2021b. Orbital Debris Quarterly News,. 25, 1–14. Pub. NASA, Orbital Debris Program Office, Houston (USA).

Neish, M.J., Deshpande, S.P., Kibe, S., Yano, H., Kitazawa, Y., Yamamoto, S., 1997. Micrometeoroid and Space Debris Impacts on the Space Flyer Unit, and Hypervelocity Impact calibration of its Materials. In: Proceedings of the Second European Conference on Space Debris. European Space Agency Spec., ESA-SP-393. pp. 177–182.

Neish, M. J., Kibe, S., 2001. Hypervelocity Impact Damage Equations for Kapton Multi-Layered Insulation and Teflon Second-Surface Mirrors. In: Proceedings of the 3rd European Conference on Space Debris. pp. 1–6.

Pailer, N., Grün, E., 1980. The penetration limit of thin films. Planet. Space Sci. 28, 321–331. https://doi.org/10.1016/0032-0633(80)90021-5.

Schimmerohn, M., Ledford, N., Putzar, R., Horch, C., Busch, S., Millinger, M., Schafer, F., 2021. LARID: Concept of a Large Area Low Resource Integrated Impact Detector. Presented at the 19th IAA Symposium on Space Debris, Dubai (United Arab Emirates). 2 pages. URL: https://iafastro.directory/iac/paper/id/63926/summary/.

Simpson, J.A., Sagdeev, R.Z., Tuzzolino, A.J., Perkins, M.A., Ksanfomality, L.V., Rabinowitz, D., Lentz, G.A., Afonin, V.V., Erö, J., Keppler, E., Kosorokov, J., Petrova, E., Szabó, L., Umlauft, G., 1986. Dust counter and mass analyser (DUCMA) measurements of comet Halley's coma from vega spacecraft. Nature 321, 278–280. https://doi.org/10.1038/321278a0.

Simpson, J.A., Tuzzolino, A.J., 1989. Cosmic dust investigations. II. Instruments for measurement of particle trajectory, velocity and mass. Nuclear Inst. Methods Phys. Res., A 279, 625–639. https://doi.org/10.1016/0168-9002(89)91312-0.

Smith, C.H., Mckinley, I.M., Ramsey, P.G., Rodriguez, J.I., 2016. Performance of Multi-Layer Insulation for Spacecraft Instruments at Cryogenic Temperatures. In The 46th International Conference on Environmental Systems. Vienna (Austria), ICES-2016-8, pp. 1–20. URL: https://ttu-ir.tdl.org/bitstream/handle/2346/67473/ICES_2016_8.pdf?sequence=1&isAllowed=y.

Srama, R., Ahrens, T.J., Altobelli, N., Auer, S., Bradley, J.G., Burton, M., Dikarev, V.V., Economu, T., Fechtig, H., Gorlich, M., Grande, M., Graps, A., Grun, E., Havnes, O., Helfert, S., Horanyi, M., Igenbergs, E., Jessberger, E.K., Johnson, T. V., Kempf, S., et al., 2004. THE CASSINI COSMIC DUST ANALYZER. Space Sci. Rev., 114, 465–518.

Strub, P., Sterken, V.J., Soja, R., Krüger, H., Grün, E., Srama, R., 2019. Heliospheric modulation of the interstellar dust flow on to Earth.

Astron. Astrophys. 621, 1–16. https://doi.org/10.1051/0004-6361/201832644, arXiv:1811.05860.

Tuzzolino, A.J., Economou, T.E., McKibben, R.B., Simpson, J.A., McDonnell, J.A., Burchell, M.J., Vaughan, B.A., Tsou, P., Hanner, M.S., Clark, B.C., Brownlee, D.E., 2003. Dust Flux Monitor Instrument for the Stardust mission to comet Wild 2. J. Geophys. Res. E: Planets 108 (10). https://doi.org/10.1029/2003je002086, paper number 8115.

Tuzzolino, A.J., McKibben, R.B., Simpson, J.A., BenZvi, S., Voss, H.D., Gursky, H., 2001. The Space Dust (SPADUS) instrument aboard the Earth-orbiting ARGOS spacecraft: I - Instrument description. Planet. Space Sci. 49, 689–703. https://doi.org/10.1016/S0032-0633(01)00012-5.

Wozniakiewicz, P., 2017. Cosmic dust in space and on Earth. Astron. Geophys., 58, 1.35–1.40. https://doi.org/10.1093/astrogeo/atx027.

Wozniakiewicz, P.J., Burchell, M.J., 2019. Space dust and debris near the Earth. Astron. Geophys 60, 38–42. https://doi.org/10.1093/astrogeo/atz150.